



HAL
open science

Guided Crystallization of Zeolite Beads Composed of ZSM-12 Nanosponges

Kassem Moukahhal, Ludovic Josien, Habiba Nouali, Joumana Toufaily,
Tayssir Hamieh, T Jean Daou, Bénédicte Lebeau

► **To cite this version:**

Kassem Moukahhal, Ludovic Josien, Habiba Nouali, Joumana Toufaily, Tayssir Hamieh, et al..
Guided Crystallization of Zeolite Beads Composed of ZSM-12 Nanosponges. *Crystals*, 2020, 10,
10.3390/cryst10090828 . hal-03060106

HAL Id: hal-03060106

<https://hal.science/hal-03060106>






Submitted on 13 Dec 2020

HAL is a multi-disciplinary open access archive for the deposit and dissemination of scientific research documents, whether they are published or not. The documents may come from teaching and research institutions in France or abroad, or from public or private research centers.

L'archive ouverte pluridisciplinaire **HAL**, est destinée au dépôt et à la diffusion de documents scientifiques de niveau recherche, publiés ou non, émanant des établissements d'enseignement et de recherche français ou étrangers, des laboratoires publics ou privés.

Article

Guided Crystallization of Zeolite Beads Composed of ZSM-12 Nanosponges

Kassem Moukahhal ^{1,2,3}, Ludovic Josien ^{1,2}, Habiba Nouali ^{1,2}, Joumana Toufaily ³,
Tayssir Hamieh ³, T. Jean Daou ^{1,2,*} and Bénédicte Lebeau ^{1,2,*}

¹ Université de Haute Alsace (UHA), CNRS, Axe Matériaux à Porosité Contrôlée (MPC), IS2M UMR 7361, F-68100 Mulhouse, France; kassem.moukahhal@uha.fr (K.M.); ludovic.josien@uha.fr (L.J.); habiba.nouali@uha.fr (H.N.)

² Université de Strasbourg, F-67000 Strasbourg, France

³ Laboratory of Materials, Catalysis, Environment and Analytical Methods Faculty of Sciences, Section I, Lebanese University Campus Rafic Hariri, Hadath, Lebanon; joumana.toufaily@ul.edu.lb (J.T.); tayssir.hamieh@ul.edu.lb (T.H.)

* Correspondence: jean.daou@uha.fr (T.J.D.); benedicte.lebeau@uha.fr (B.L.);
Tel.: +33-389336739 (T.J.D.); +33-389336882 (B.L.)

Received: 24 August 2020; Accepted: 15 September 2020; Published: 17 September 2020



Abstract: The direct route using a bifunctional amphiphilic structuring agent for the synthesis of hierarchical nanozeolites coupled with pseudomorphic transformation was used for the crystallization of hierarchized zeolite beads/hollow spheres composed of ZSM-12 (MTW structural-type) with nanosponge morphology. These beads/hollow spheres have the same average diameter of 20 μm as their counterpart amorphous mesoporous silica beads used as precursor in the starting synthesis mixture. The effects of synthesis parameters, such as stirring and treatment time at 140 $^{\circ}\text{C}$, on the morphology, structure, and texture of the materials have been investigated using X-ray diffraction (XRD), N_2 sorption, scanning electronic microscopy (SEM), and transmission electronic microscopy (TEM) techniques. Static conditions were found necessary to maintain the morphology of the starting amorphous silica beads. An Ostwald ripening phenomenon was observed with the increase in hydrothermal treatment time leading to the dissolution of the interior of some beads to form core shell beads or hollow spheres with larger crystals on the outer surface. These ZSM-12 beads/hollow spheres possess higher porous volume than conventional ZSM-12 zeolite powder and can be used directly for industrial applications.

Keywords: zeolite beads; hierarchical zeolite; pseudomorphic transformation; ZSM-12; shaping; nanosponges

1. Introduction

Zeolites constitute a category of aluminosilicate crystals with microporous frameworks. They are good candidates for adsorption, catalysis and separation due to their shape selectivity and high thermal stability [1–6]. However, the diffusion of molecules is limited in micropores and thus the performance of zeolites in catalytic reactions or adsorption often depends strongly on the size, morphology and porosity (pore size and pore topology) of the crystals [7–10]. In catalysis, diffusional limitations often lead to coke formation or reduce the accessibility to active sites. For molecular decontamination, adsorption capacity and kinetics are mainly governed by pore size and porous volume. Zeolites having a one-dimensional (1D) pore system, such as MTW, TON, or MOR type, and generally suffer from a long diffusion path in crystals with high aspect ratios (length/width) and pore channels oriented along the length [11]. In recent years, a particular attention has been brought to rationally design

the crystal morphology and/or the porosity of a given zeolite in order to reduce diffusion path in microporosity [12]. In this context, the reduction of crystal size or introducing larger pores appeared the best strategies. Post-treatments consisting in dealumination or desilication are the conventional methods for generating mesopores within zeolite crystals [13–16]. The crystallization of zeolites with hierarchical micro/mesoporous structures by using bifunctional amphiphilic structure directing agent was also identified as a performant alternative [9,17–26]. Moreover, the addition of additives, such as crystal growth modifiers [27–29] or seed crystals (salt-aided seed-induced route) [8,30], also makes it possible to tailor the size and the morphology of the crystals by inhibiting the crystal growth along certain specific network planes or by controlling the process of dissolution-recrystallization, respectively.

ZSM-12 zeolite of MTW-type is a highly silicic 1D-pore system with a framework Si/Al molar ratio always higher than 20, and has shown interesting features for acid catalysis such as high coking resistance and high chemical stability [31]. It was first synthesized by Rosinski and Rubin [32] in a reaction medium containing diethyl sulphate and triethylamine. In 1985, LaPierre et al. resolved the structure using X-ray powder diffraction [33]. The unit cell is monoclinic, the space group is C2/m and the unit cell parameters are: $a = 24.88$, $b = 5.02$ Å, $c = 12.15$ Å, and $\beta = 107.7^\circ$. The structure contains rings with four, five, and six T atoms (T = Si or Al) and has a one-dimensional system of channels with 12 T atoms with pore openings of $\sim 5.6 \times 6.1$ Å. Looking at the structure in a direction perpendicular to the axis of the channels we can observe that the walls are formed only by six-atom rings T with an opening of about 2.5 Å. This small opening prevents the passage of adsorbed molecules between the channels [34]. As a consequence, ZSM-12 zeolite is characterized by non-interconnecting tubular-like linear channels that were identified to be responsible for not allowing the accumulation of coking precursors [31].

The particular micropores dimensions of the ZSM-12 zeolite, make it performant catalyst in reactions involving cyclic hydrocarbons. Pazzucconi et al. used ZSM-12 zeolite for alkylation of naphthalene in liquid phase at high pressure in the presence of 1,2,4-trimethylbenzene as a solvent, and they reported a high activity and high selectivity of ZSM-12 zeolite to 2,6-dimethylnaphthalene [35,36]. Higher stability and higher activity on the reaction time in the catalytic cracking of naphthalene were observed on ZSM-12 zeolite, which can provide insight into the catalytic performance for many reactions. However, ZSM-12 zeolite also suffers diffusional limitations in micropores and the hierarchization of the pore network was investigated and revealed beneficial to improve its catalytic performance.

Dugkhuntod et al. recently reported the synthesis of hierarchical ZSM-12 nanolayers via a dual template method [37]. Hierarchical ZSM-12 nanolayers exhibit an improvement of catalytic activity in terms of levulinic acid conversion compared to other hierarchical zeolite nanosheets, such as MFI (ZSM-5) and FAU. The better catalytic performance was related to the enhanced mesoporosity and the presence of a large one-dimensional 12-membered ring network, which can promote the accessibility of bulky-molecules to active sites of zeolite.

Zeolites or hierarchized zeolites synthesized with conventional hydrothermal routes leads to micrometer-sized crystals or nanocrystal aggregates, respectively, forming fine powder products. However, the use of these materials in powder form can be disadvantageous for certain industrial applications such as those based on continuous flow processes. Indeed, they can generate too much pressure drop and cause clogging of the cartridges/columns/filters used on an industrial scale. Moreover, these zeolite powders can be a source of secondary contamination and often fine powders causes problems of handling (due to particles spreading). Therefore, the development of methods for shaping these materials into objects of controllable shape and size is of great technological importance. However, shaping methods of zeolite powder usually require several steps such as compacting, grinding and sieving for obtaining grains of similar size, or assembling the zeolite particles by extrusion or mixing in presence of organic (e.g., polymers) or inorganic (e.g., clays, sodium silicate) binders, which can reduce the performance of the zeolite materials [38–40], or removal of sacrificial macrotemplates (resin, ...) [41,42]. A one-step and binderless process such as pseudomorphic transformation is an interesting alternative for shaping zeolite powder. This strategy consists by controlling the

dissolution/crystallization process to transform a shaped material into another one having different chemical composition but the same shape. This concept was successfully used by Anne Galarneau's team to synthesize micrometric beads and zeolite monoliths of the LTA, SOD and FAU type with low Si/Al ratios [43–46]. Our group has recently reported the direct synthesis of hierarchical ZSM-5 beads [47] and monoliths with nanosheets morphology [48], and also plain and hollow purely silica beads of silicalite-1 nanosheets by using the pseudomorphic transformation method [49]. Here, we report the use of the pseudomorphic transformation concept to elaborate hierarchical ZSM-12 zeolite beads with nanosponges morphology thanks to the use of a dual-porogenic surfactant as a template and growth inhibitor, which was used for zeolite *BEA nanosponge synthesis [9,21,25].

2. Materials and Methods

2.1. Preparation of ZSM-12 Beads

2.1.1. Synthesis of the Dual-Porogenic Surfactant Template

The dual-porogenic surfactant $C_{22}H_{45}-N^+(CH_3)_2-C_6H_{12}-N^+(CH_3)_2-CH_2-Phe-CH_2-N^+(CH_3)_2-C_6H_{12}-N^+(CH_3)_2-CH_2-Phe-CH_2-N^+(CH_3)_2-C_6H_{12}-N^+(CH_3)_2-C_{22}H_{45}$, $(Br^-)_2(Cl^-)_4$, (abbreviated as N₆-Diphe, Phe = C₆H₄) have been used to generate ZSM-12 nanosponges beads and hollow spheres. This surfactant has been synthesized in three steps following the procedure described by Na et al. [21]. 16.2 g (0.01 mol) of 1-bromodocosane (TCI EUROPE N.V., Zwijndrecht, Belgium) and 68.8 g (0.1 mol) of N,N,N',N'-tetramethyl-1,6-diaminohexane (Sigma-Aldrich Chemie S.a.r.l., Saint-Quentin Fallavier, France) were dissolved in 400 mL of acetonitrile/toluene mixture (1:1 vol/vol) and heated under reflux at 70 °C for 12 h with magnetic stirring. After cooling to room temperature, the solvent was evaporated by rotary evaporator, and the product was filtered, washed with diethyl ether, and dried under vacuum at 50 °C. The product obtained was denoted C₂₂₋₆₋₀.

In a second step, 8 g of C₂₂₋₆₋₀ (0.01 mol) and 23.56 g (0.1 mol) of α,α' -dichloro-p-xylene (Sigma-Aldrich Chemie S.a.r.l., Saint-Quentin Fallavier, France) were dissolved in 100 mL of acetonitrile, which were heated to 60 °C for 48 h with magnetic stirring. After evaporation of the organic solvent by rotary evaporator, the solid product of the formula $C_{22}H_{45}-N^+(CH_3)_2-C_6H_{12}-N^+(CH_3)_2-CH_2-(p-C_6H_4)-CH_2-Cl(Br^-)(Cl^-)$, designated C_{22-6-phe-Cl}, was precipitated. This product was washed with diethyl ether, filtered, and dried under vacuum at 50 °C. Finally, 10 g (0.02 mol) of C_{22-6-phe-Cl} and 1.12 g (0.01 mol) of N,N,N',N'-tetramethyl-1,6-diaminohexane (Sigma-Aldrich Chemie S.a.r.l., Saint-Quentin Fallavier, France) were dissolved in 100 mL of chloroform and refluxed for 24 h under magnetic agitation. The solvent was evaporated by rotary evaporator and a final solid product (N₆-diphe) was recovered. The solid was washed with diethyl ether, filtered, and dried under vacuum at 50 °C. The yield was 80%.

Purity was checked by ¹H liquid nuclear magnetic resonance (NMR), the chemical shifts obtained are as follows: ¹H NMR (CDCl₃, 400 MHz, 25 °C): δ (ppm) [C3] 0.83 (m, 6H); 1.3 (m, 41H); 1.59 (s, 4H); 1.71 (s, 4H); 2.01 (s, 3H); [C2] 3.36 (s, 12H); [C1] 3.47 (m, 4H); 3.72 (m, 4H).

2.1.2. Synthesis of ZSM-12 Nanosponges Beads

First, 0.3 g of sodium hydroxide (NaOH 99%, Carlo Erba Reagents, Val-de-Reuil, France) and 0.037 g sodium aluminate (NaAlO₂ 92%, Strem Chemicals, Inc., Bischeim, France) were dissolved in 21.3 g of distilled water. Then, 6.14 g of pure ethanol (ETOH, 99%, VWR International S.A.S, Fontenay-sous-Bois, France) and 1.6 g of the dual-porogenic surfactant the N₆-Diphe were added to the previous mixture. In a next step, the obtained mixture was mixed with 1 g of amorphous mesoporous silica beads with an average size of 20 μ m (data given by the supplier SiliCycle Inc., Quebec, Canada) to set the molar composition to: 1 SiO₂: 0.22 Na₂O: 0.0125 Al₂O₃: 0.05 N₆-Diphe: 8 EtOH: 71 H₂O. The resulting precursor gel was introduced in a PTFE[®]-lined stainless-steel autoclave of 45 mL for crystallization at 140 °C for 4 days under tumbling conditions at 60 rpm or under static mode for several

days (4, 5, 7, 14 and 21 days). The final product is recovered by filtration, then washed with distilled water before drying for 12 h at 80 °C. The dual porogenic surfactant was eliminated by calcination under air at 550 °C for 8 h.

The synthesized samples are denoted t-S, or t-NS, where “t” stands for the hydrothermal treatment time at 140 °C, and “S” or “NS” means that the samples was synthesized under tumbling stirring or not (static mode), respectively

2.2. Characterization of Zeolite Beads

The purity and crystallinity of the obtained samples was checked by X-ray diffraction (XRD). The samples were introduced in glass capillaries and the X-ray patterns were recorded using a STOE STADI-P (STOE & Cie GmbH, Darmstadt, Germany) diffractometer using Cu K α ₁ radiation ($\lambda = 0.15406$ nm) in the range $3^\circ < 2\theta < 50^\circ$.

Scanning and transmission electron microscopy (SEM and TEM) were performed to analyze morphology, homogeneity, and particle sizes. Philips XL30 FEG (Field Emission Gun) (Philips, Verduin, France) and JEOL JSM-7900F (JEOL, Val-de-Reuil, France) scanning electron microscopes (SEM) were used. The later was equipped with a BRUKER QUANTAX spectrometer (BRUKER, Champs sur Marne, France) for the energy dispersive X-ray analyses (EDX). The transmission electron microscopy (TEM) was carried out on a JEOL (Val-de-Reuil, France) model ARM 200, operating at 200 kV, with a point-to-point resolution of 80 pm. For EDX analyses, samples were previously embedded in an epoxy resin for cold mounting (EpoFix from Struer S.A.S. Champigny sur Marne, France), which was grinded with various grinding papers and then polished until a soft surface was obtained.

Nitrogen sorption isotherms were recorded at -196 °C using a Micromeritics (Merignac, France) sorptometer (model ASAP 2420). In prior analyses, the samples were out-gassed under vacuum at 300 °C for 15 h. The BET method was used for determining the specific surface area. The total pore volume was determined from the total amount of N₂ adsorbed at saturation (i.e., at $p/p^\circ = 0.99$ in absence of textural porosity). The Density Functional Method (DFT) method was applied on the adsorption branch in order to obtain the pore size distributions [50]. The microporous volumes were calculated by using a modified t-plot method.

The amounts of dual porogenic agent occluded within the porosity of sample were determined by thermogravimetric analysis (METTLER TOLEDO, Viroflay, France, model TG/DSC STARe) from 20 to 800 °C under air with a heating rate of 5 °C/min⁻¹.

The Si/Al molar ratios were determined using X-ray fluorescence spectrometry (XRF) performed on a PANalytical (Limeil-Brévannes, France) equipment model Zetium and from EDX analyses.

3. Results and Discussion

The purity and crystallinity of the synthesized zeolites were investigated by X-ray diffraction (Figure 1). The X-ray patterns of the all obtained materials present diffraction peaks, which correspond to a pure phase of ZSM-12 zeolite in agreement with the corresponding patterns available in the literature [51]. The diffraction peaks are broader for samples hydrothermally treated under static conditions for 4, 5 and 7 days (4-NS, 5-NS and 7-NS, respectively), which indicate a small crystal size and/or a low crystallinity degree. The thinner diffraction peaks with higher intensity observed after 4 days of hydrothermal treatment with mechanical stirring (4-S) and after 14 and 21 days in static mode (14-NS and 21-NS, respectively) indicate the presence of larger crystal sizes and/or high crystallinity degree.

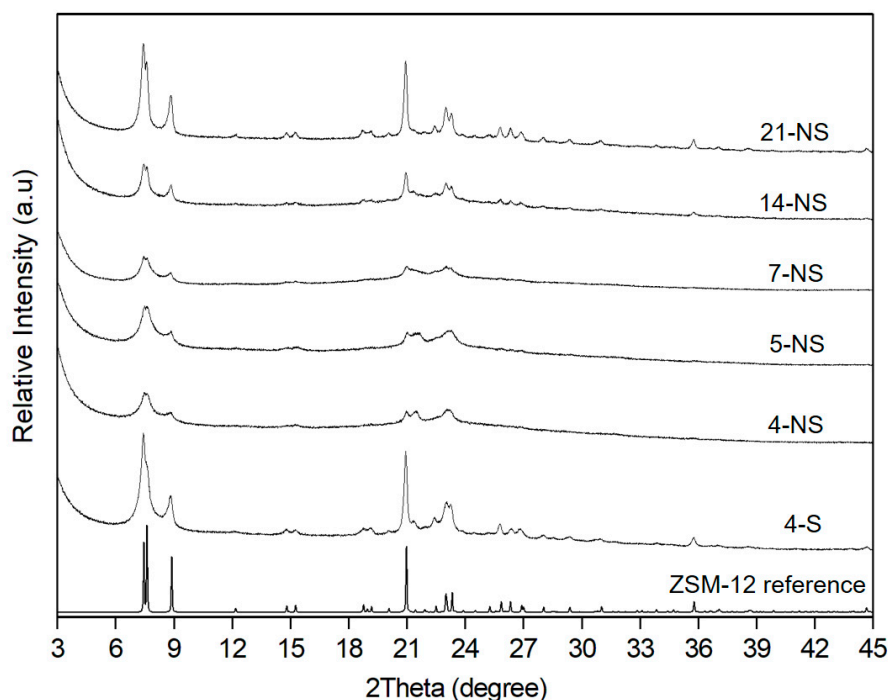


Figure 1. XRD patterns of the calcined ZSM-12 zeolites obtained by pseudomorphic transformation and XRD reference pattern of ZSM-12 zeolite [51].

SEM images displayed in Figure 2 show that the morphology of the parent silica beads (Figure S1) has been totally lost for the sample 4-S synthesized under stirring (Figure 2a). However, the nanosponge morphology was observed by TEM (Figure 3a). Indeed, TEM image show nano-sized zeolite crystals delimiting mesopores with narrow pore size distribution as a result of the self-assembly of the long hydrocarbon chains of the multiammonium surfactant used as structure directing agent. This, in complement of XRD data, indicates that stirring favor a fast crystallization of ZSM-12 nanosponges but induce the loss of the parent bead morphology. On the other hand, the spherical morphology of the parent amorphous silica beads was maintained when the hydrothermal treatment was carried out in static mode for all investigated durations (Figure 2b–f). The breaking of the beads upon stirring allowed a faster diffusion of reactants present in the liquid phase (aluminum source, bifunctional structuring agent N_6 -Diphe) to the silica backbone compared to the plain beads. SEM images at high magnification displayed in Figure 2 show that beads are constituted of spherical agglomerates of ZSM-12 nanocrystals, with an average of 400 ± 90 nm diameter after four and five days of hydrothermal treatment. The size of the agglomerates of ZSM-12 nanocrystals seems to increase slightly to reach about 1 ± 0.2 μm by increasing the duration of the hydrothermal treatment to seven and 14 days, and reaches about 1.7 ± 0.2 μm after 21 days. In parallel, the size ZSM-12 nanocrystals composing these agglomerates increases from 4 nm (4-S and 4-NS samples) to reach a maximum of 80 nm after 21 days of hydrothermal treatment as shown in Figure 3a,b. The nanocrystal size distribution seems also to increase while increase the hydrothermal treatment time, especially for 7-NS, 14-NS and 21-NS samples (Figure 3c–e). These results are consistent with the sharper X-ray diffractions peaks when increasing the time of the hydrothermal treatment. According to the TEM images of samples 4-S, 4-NS, 7-NS, 14-NS, and 21-NS displayed in Figure 3, nanosponges are composed by randomly agglomerated nanocrystals interconnected by mesopores, which are characteristic of nanosponge morphology [9,25]. Since beads have been crushed for TEM observations, it is difficult to identify the location of the crystals of different sizes in the obtained beads. However, by correlation with SEM observations these big crystals are probably located at the outer surface of the beads while small ones are inside as already observed in our previous work on the synthesis of silicalite-1 zeolite beads and hollow spheres,

where the crystallization seems to begin on the external surface of the beads and to diffuse with the time inside the beads [49].

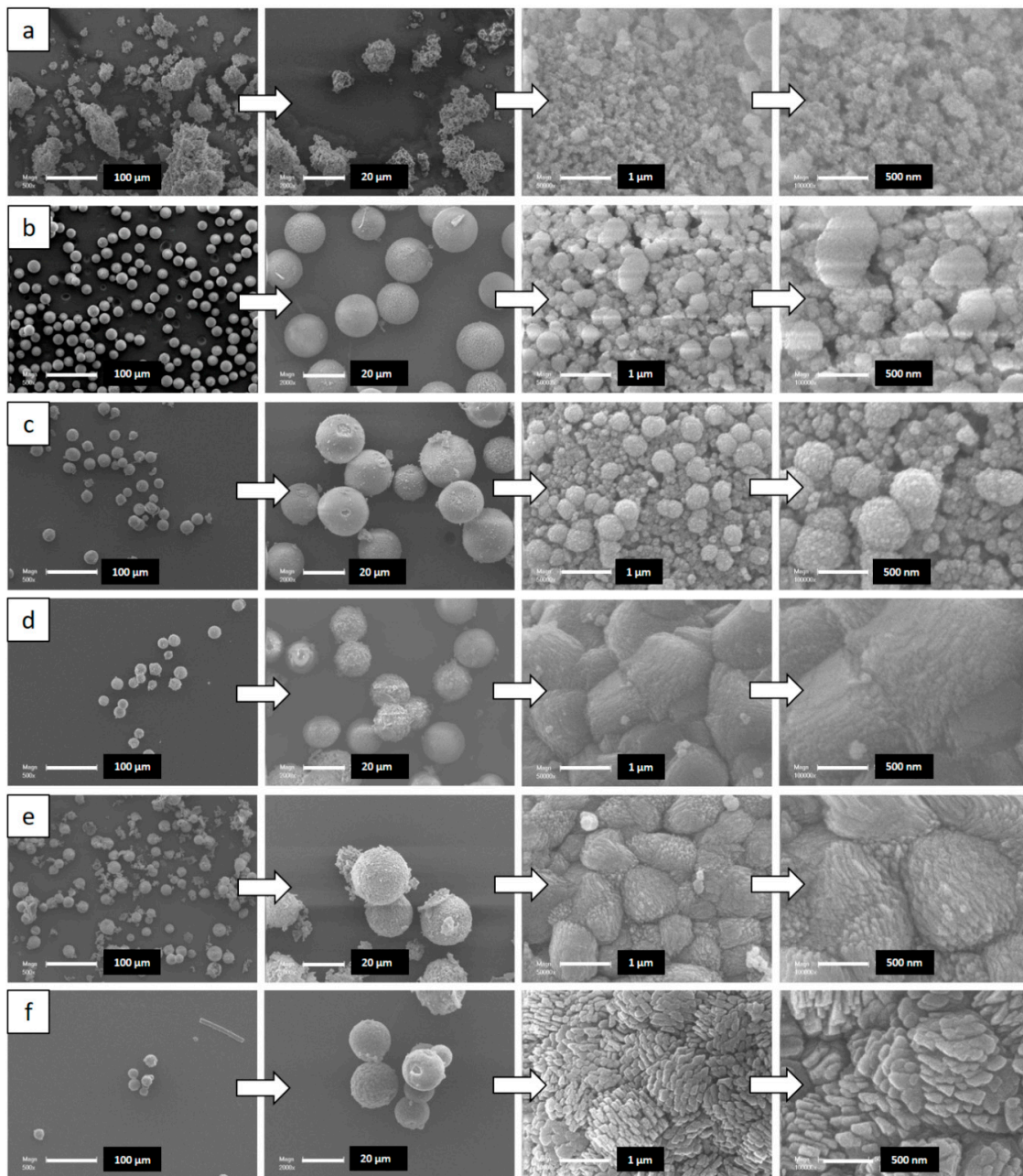


Figure 2. SEM images of all samples (a) 4-S (b) 4-NS (c) 5-NS (d) 7-NS (e) 14-NS (f) 21-NS obtained after the pseudomorphic transformation of the amorphous silica beads.

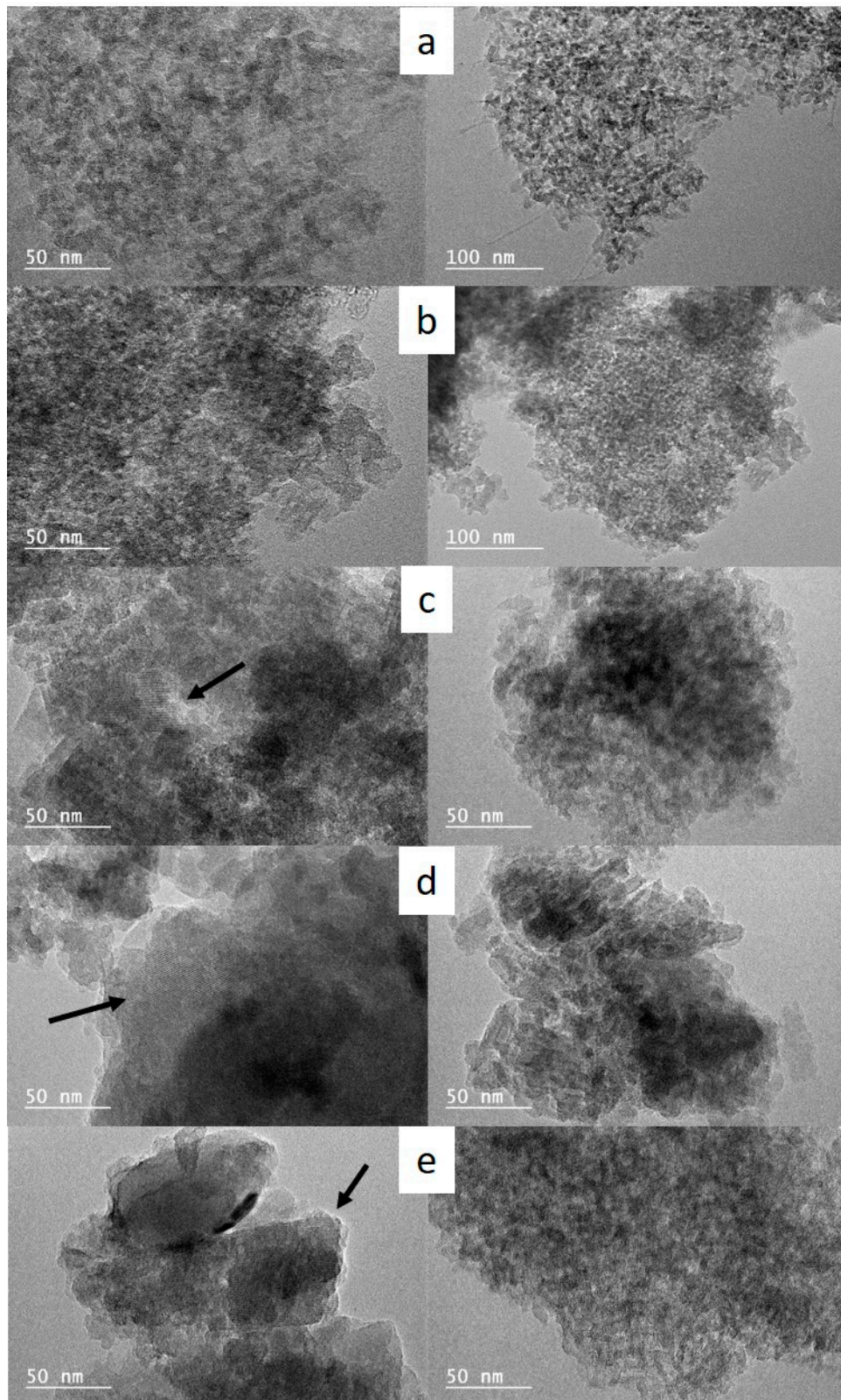


Figure 3. TEM images of (a) 4-S (b) 4-NS (c) 7-NS (d) 14-NS (e) 21-NS samples showing the morphology of the obtained hierarchized ZSM-12 zeolites (Black arrows indicate the presence of larger crystals).

The nitrogen adsorption-desorption isotherms at 77 K of the calcined materials are shown in Figure 4a. The nitrogen adsorption-desorption isotherm of the parent silica beads is of type IV (according to an IUPAC classification) (Figure S2) [52]. For the samples obtained by pseudomorphic transformation, isotherms are a mixture of type I (low relative pressure p/p°) and type IV (high p/p°). All isotherms present a H3 hysteresis in the $0.4 < p/p^\circ < 1$ range, which is characteristic of mesoporosity induced by the alkyl chains and the phenyl groups of the dual-porogenic surfactant (N6-Diphe). However, for 4-S and 4-NS samples, some interparticle mesoporosity is also clearly observed (type II at high p/p°). The type I shape of the isotherms is coherent with the presence of the micropores. The textural properties of all materials determined from the nitrogen adsorption-desorption isotherms are presented in Table 1. The microporous volumes have been determined by the t-plot method with the correction proposed by Galarneau et al. for hierarchical zeolites [53,54]. The microporous volume of the sample 4-S, where the morphology of the starting beads is not conserved, is $0.19 \text{ cm}^3/\text{g}$. A lower microporous volume ($0.15 \text{ cm}^3/\text{g}$) has been measured for the sample synthesized with the same duration (4 days) but under static conditions. These microporous volumes are higher than the one expected for conventional ZSM-12 zeolite ($0.05\text{--}0.11 \text{ cm}^3/\text{g}$) [37,55,56] because of the presence of secondary micropores with a diameter of 1.5 nm revealed by the pore size distribution obtained by applying DFT Method [50] (Figure 4b). The volume of these secondary micropores seem to decrease by increasing the hydrothermal treatment time. It is assumed that they were generated by the presence of dual-porogenic surfactant N6-Diphe. Indeed, such secondary microporosity generated by this kind of bifunctional amphiphilic structuring agent was already observed in hierarchized ZSM-5 [47]. It is noteworthy that secondary micropores of the same size are also present in the parent amorphous silica beads. However, no porosity was detected on as-made materials, suggesting that original secondary micropores (due to amorphous silica beads) disappeared upon pseudomorphic transformation. The total microporous volume decreases to about $0.11\text{--}0.13 \text{ cm}^3/\text{g}$ with the increase of the hydrothermal treatment time (5 days and more). This phenomenon can be explained by “Ostwald ripening” when small crystals are used as nutriment to give birth to bigger ones. This assumption is consistent with SEM and TEM observations, and with the thinner diffraction peaks obtained by XRD. Figure 4b shows the presence of mesopores of about 5 nm in average diameter with a wide mesopore size distribution going from 2 to 15 nm for the obtained samples. These mesopores do not come from the parent amorphous silica beads since these latter have also a large pore size distribution but centered at 10 nm (Figure S1). They are formed by the micellization of the hydrophobic long chains of dual structure directing agents and are responsible of the nanosponge morphology. It is noteworthy that mesoporous volumes (without interparticle porosity for 4-NS sample) increase linearly with the hydrothermal treatment time (Figure 5).

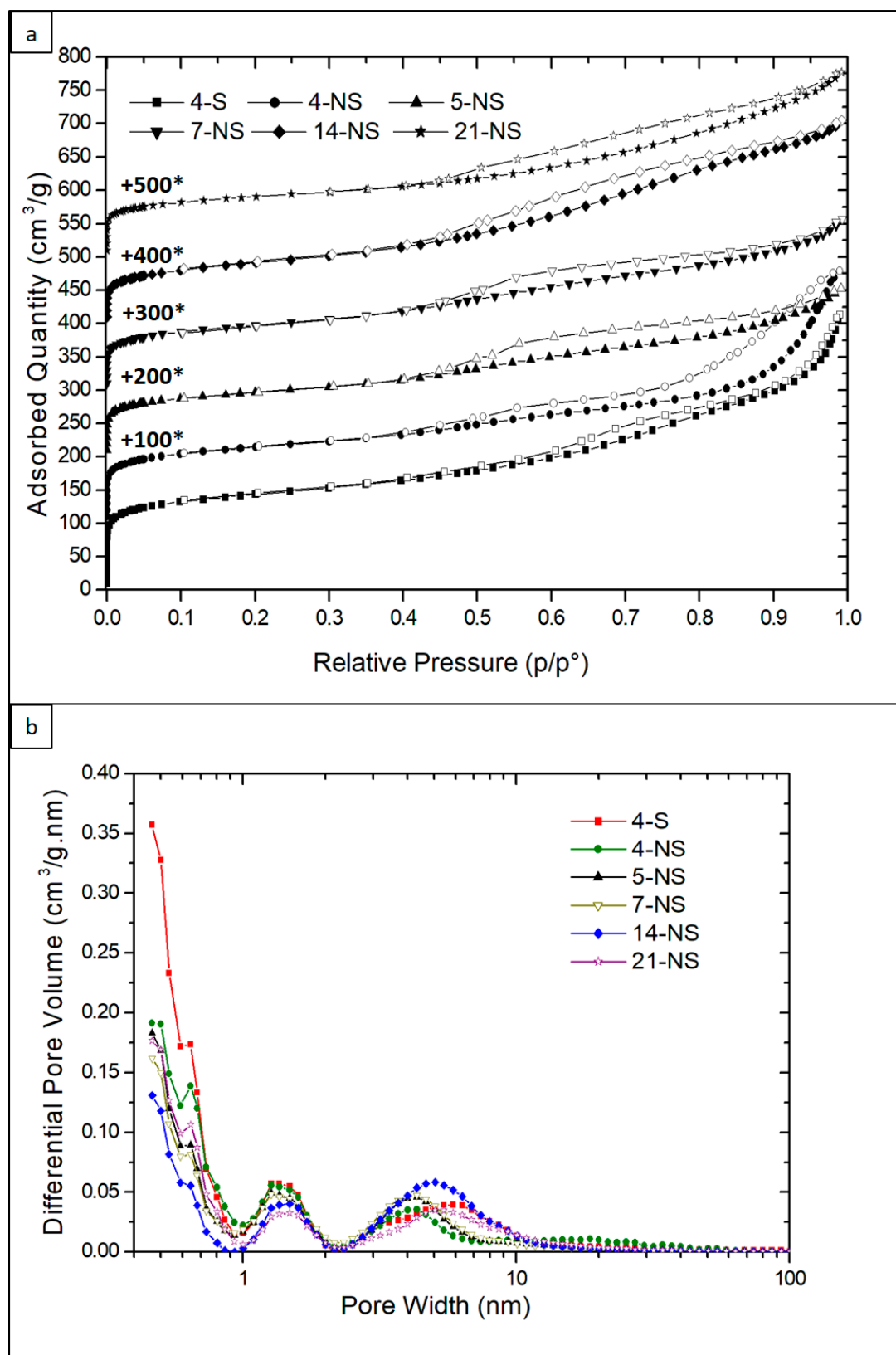
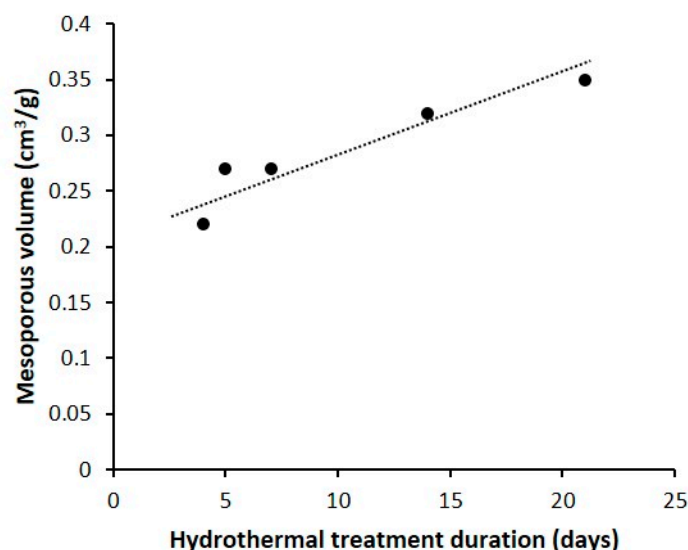


Figure 4. (a) N₂ isotherms sorption at 77 K and (b) pore size distributions for all the calcined samples obtained after pseudomorphic transformation. (*) For clarity reason, isotherms have been shifted along y-axis and these values (in cm³/g) are the used increments.

Table 1. Textural properties of the calcined obtained samples and weight losses determined by TGA on as-made samples.

	SBET ^a (m ² /g)	V _{tot} ^b (cm ³ /g)	V _{micro} ^c (cm ³ /g)	V _{meso} ^d (cm ³ /g)	Mesopores Diameter ^e (nm)	Physisorbed Water (%) ^f	Organic Matter (%) ^g
4-S	498	0.51 (0.42) *	0.19	0.32 (0.23) **	5.5	2.6	26
4-NS	417	0.59 (0.37) *	0.15	0.44 (0.22) **	5.8	3.8	22
5-NS	351	0.39	0.12	0.27	4.2	3.3	24.5
7-NS	347	0.40	0.13	0.27	4.1	3.6	24.8
14-NS	328	0.43	0.11	0.32	5.6	4.2	34.1
21-NS	327	0.47	0.12	0.35	4.5	2.6	38.5

^a Determined by using BET (Brunauer-Emmet-Teller) method. ^b Determined at $p/p^\circ = 0.99$. * value corresponding to the total pore volume determined on the plateau after hysteresis at $p/p^\circ = 0.91$ without interparticle porosity. ^c Determined with corrected t-plot method [53,54]. ^d $V_{meso} = V_{tot} - V_{micro}$. ** value calculated with V_{tot} determined at $p/p^\circ = 0.91$. ^e Determined from pore size distributions. ^f Weight loss determined by TGA in the temperature range 30–120 °C. ^g Weight loss determined by TGA in the temperature range 120–700 °C.

**Figure 5.** Evolution of the mesoporous volume of 4-NS, 5-NS, 7-NS, 14-NS and 21-NS samples (without interparticle porosity for 4-NS sample) with the hydrothermal treatment duration.

TGA analysis under air done on the as-synthesized samples shows 2 weight losses: a small one between 30 and 120 °C corresponding to the physisorbed water and a large one between 120 and 700 °C corresponding to the oxidation of the dual-porogenic surfactant used for the synthesis (Table 1). As well as the mesoporous volume, the amount of dual-porogenic surfactant determined by TGA increases linearly with the hydrothermal treatment time (Figure 6). This indicates that the incorporation of the dual porogenic surfactant N6-Diphe increases with the hydrothermal treatment time, resulting in a higher internal mesopore volume.

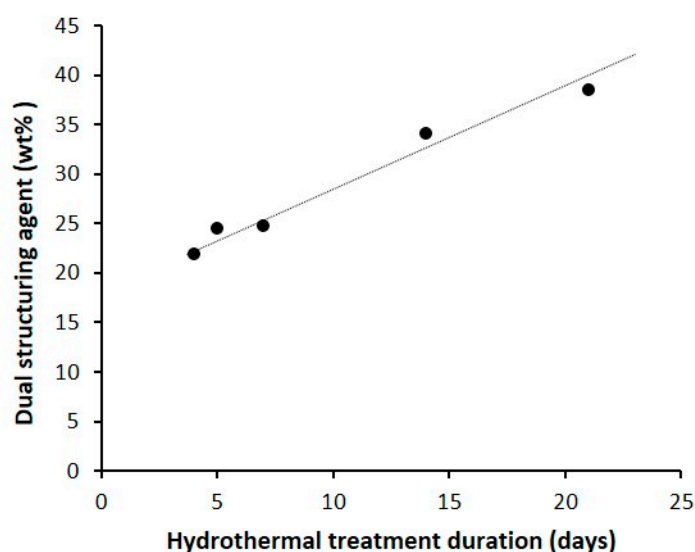


Figure 6. Evolution of the weight percentage of the dual structuring agent determined by TGA of 4-NS, 5-NS, 7-NS, 14-NS and 21-NS samples with the hydrothermal treatment duration.

In order to study the evolution of the inner part of the spheres and the silica and aluminum distribution as function of the hydrothermal treatment time, SEM observations and EDX analyses (Figure 7) were performed on three of the synthesized samples. For that, it was necessary to prepare cross section of the beads by embedding the samples in resin and then polish them. After four days of hydrothermal treatment in static mode, beads are plain, and the distribution of silica and aluminum is homogeneous on the whole of the bead indicating the nanocrystals formation in the whole beads. When increasing the duration of treatment to seven days, core-shell beads are mainly observed with a more important silica content in the shell than in the core. Few hollow spheres are also observed indicating the partial dissolution of the bead center. After 21 days, core-shell beads are still observed in coexistence with a higher number of hollow spheres. These observations are consistent with the assumption that the crystallization begins from the outer surface and propagates to the center, and with time the interior of the beads dissolve to feed the growth of the crystals located at the surface of the shell. From EDX analyses performed on all ZSM-12 nanosponges beads and hollow spheres, an average value of 30 was determined for the Si/Al ratio, which is close to the average value of 35 determined by XRF. These values are coherent with the initial Si/Al molar ratio of the precursor gel that was 40.

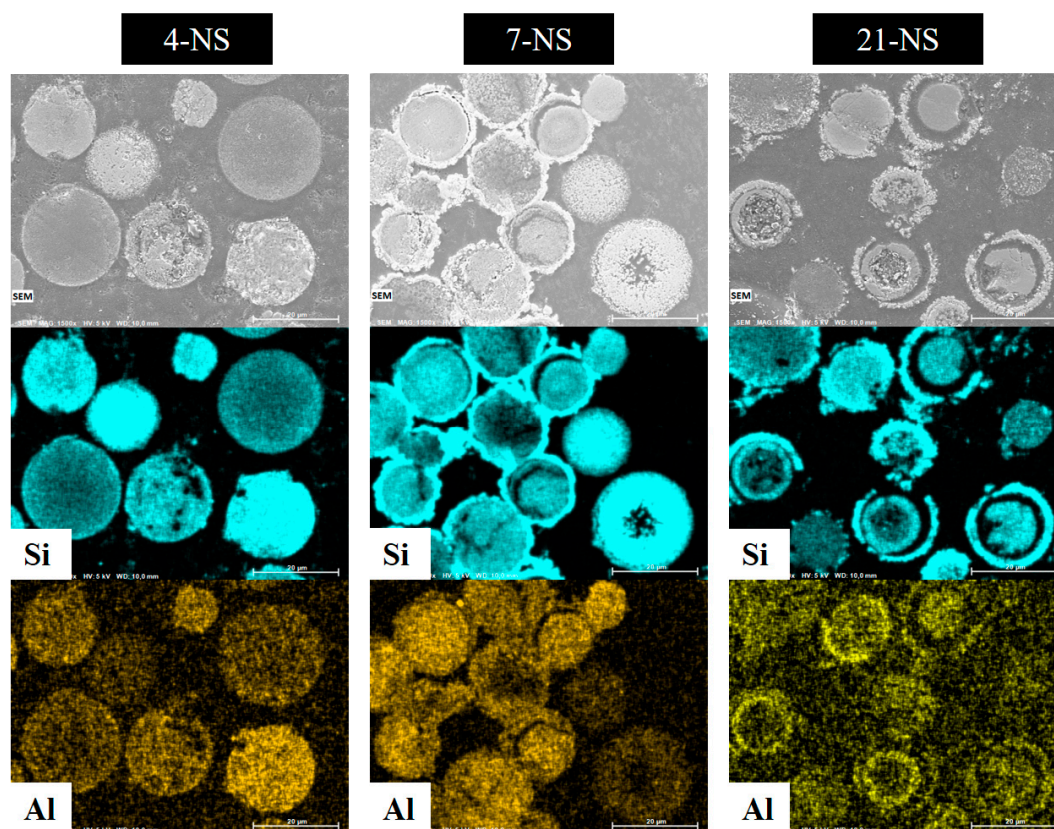


Figure 7. SEM images and corresponding EDX element mapping (Si and Al) for the samples 4-NS, 7-NS and 21-NS.

4. Conclusions

The pseudomorphic transformation pathway was applied for the synthesis of 20- μm beads composed of ZSM-12 zeolite nanosponges with MTW structure type. When hydrothermal treatment was performed with mechanical stirring (4-S), the starting amorphous silica spheres were broken and the diffusion of reactants within mesopores of the starting amorphous silica beads was faster. The crystallization of the amorphous silica walls into ZSM-12 was thus faster compared to the case when hydrothermal treatment was performed under static conditions for the same duration (4-NS). In both cases, ZSM-12 nanosponges were formed as observed by TEM images but the crystallization rate is lower for 4-NS, in agreement with broader XRD peaks for this latter sample. With one additional day of hydrothermal treatment under static conditions (5-NS), the crystallization rate increases in accordance with XRD data that showed thinner peaks. After seven days of hydrothermal treatment at 140 °C under static conditions an Ostwald ripening phenomenon has started, which results in growth of the crystals located at the outer surface of the beads. These bigger crystals are responsible for the thinner peaks observed by XRD. As observed by SEM and EDX, they form a shell rich in silicon. Beads and hollow spheres are composed of ZSM-12 zeolite nanocrystals (4 to 80 nm in size) interconnected to each other through a mesoporous network giving rise to a nanosponge morphology. This morphology generates an additional porosity (mesoporosity and secondary microporosity) to the microporosity of the zeolites (total pore volume greater than the one of conventional ZSM-12 zeolite) and improves the diffusion within this material, which should result in improving the kinetics as well as the adsorption capacities and catalytic properties of this material.

Supplementary Materials: The following are available online at <http://www.mdpi.com/2073-4352/10/9/828/s1>, Figure S1. Scanning electron microscopy (SEM) images of the parent amorphous 20 μm silica spheres. An average size of $23 \pm 3 \mu\text{m}$ was determined from measurements on about 100 beads, Figure S2. (a) Nitrogen sorption isotherm at 77 K and (b) DFT pore size distribution determined from the adsorption branch of the N_2 isotherm for the parent amorphous silica beads.

Author Contributions: Conceptualization, T.J.D. and B.L.; methodology, K.M., T.J.D., J.T., and B.L.; validation, L.J. and H.N.; investigation, K.M.; data curation, K.M., T.J.D., and B.L.; writing—original draft preparation, K.M.; writing—review and editing, T.J.D. and B.L.; supervision, T.J.D., J.T., T.H., and B.L.; project administration, T.J.D. and B.L. All authors have read and agreed to the published version of the manuscript.

Funding: This research received funding from Institut Universitaire de France (IUF).

Acknowledgments: The XRD: adsorption and Electronic microscopies platforms of IS2M are acknowledged. Laure Michelin, Habiba Nouali, Ludovic Josien, and Loïc Vidal are warmly thanked for their help in XRD, N_2 adsorption–desorption, SEM and TEM acquisition data, respectively.

Conflicts of Interest: The authors declare no conflict of interest.

References

1. Dusselier, M.; Van Wouwe, P.; Dewaele, A.; Jacobs, P.A.; Sels, B.F. Shape-selective zeolite catalysis for bioplastics production. *Science* **2015**, *349*, 78–80. [[CrossRef](#)] [[PubMed](#)]
2. Zhang, R.; Liu, N.; Lei, Z.; Chen, B. Selective transformation of various nitrogen-containing exhaust gases toward N_2 over zeolite catalysts. *Chem. Rev.* **2016**, *116*, 3658–3721. [[CrossRef](#)] [[PubMed](#)]
3. Valtchev, V.; Majano, G.; Mintova, S.; Pérez-Ramírez, J. Tailored crystalline microporous materials by post-synthesis modification. *Chem. Soc. Rev.* **2013**, *42*, 263–290. [[CrossRef](#)] [[PubMed](#)]
4. Smit, B.; Maesen, T.L.M. Towards a molecular understanding of shape selectivity. *Nature* **2008**, *451*, 671–678. [[CrossRef](#)]
5. Deroche, I.; Daou, T.J.; Picard, C.; Coasne, B. Reminiscent capillarity in subnanopores. *Nat. Commun.* **2019**, *10*, 4642. [[CrossRef](#)] [[PubMed](#)]
6. Huve, J.; Ryzhikov, A.; Nouali, H.; Lalia, V.; Augé, G.; Daou, T.J. Porous sorbents for the capture of radioactive iodine compounds: A review. *RSC Adv.* **2018**, *8*, 29248–29273. [[CrossRef](#)]
7. Reddy, J.K.; Motokura, K.; Koyama, T.; Miyaji, A.; Baba, T. Effect of morphology and particle size of ZSM-5 on catalytic performance for ethylene conversion and heptane cracking. *J. Catal.* **2012**, *289*, 53–61. [[CrossRef](#)]
8. Zhang, H.; Hu, Z.; Huang, L.; Zhang, H.; Song, K.; Wang, L.; Shi, Z.; Ma, J.; Zhuang, Y.; Shen, W.; et al. dehydration of glycerol to acrolein over hierarchical ZSM-5 zeolites: Effects of mesoporosity and acidity. *ACS Catal.* **2015**, *5*, 2548–2558. [[CrossRef](#)]
9. Kabalan, I.; Lebeau, B.; Nouali, H.; Toufaily, J.; Hamieh, T.; Koubaissy, B.; Bellat, J.-P.; Daou, T.J. New generation of zeolite materials for environmental applications. *J. Phys. Chem. C* **2016**, *120*, 2688–2697. [[CrossRef](#)]
10. Astafan, A.; Pouilloux, Y.; Patarin, J.; Bats, N.; Bouchy, C.; Daou, T.J.; Pinard, L. Impact of extreme downsizing of *BEA-type zeolite crystals on n -hexadecane hydroisomerization. *New J. Chem.* **2016**, *40*, 4335–4343. [[CrossRef](#)]
11. Larlus, O.; Valtchev, V.P. Crystal morphology control of LTL-type zeolite crystals. *Chem. Mater.* **2004**, *16*, 3381–3389. [[CrossRef](#)]
12. Drews, T.O.; Tsapatsis, M. Progress in manipulating zeolite morphology and related applications. *Curr. Opin. Colloid Interface Sci.* **2005**, *10*, 233–238. [[CrossRef](#)]
13. Wakihara, T.; Ihara, A.; Inagaki, S.; Tatami, J.; Sato, K.; Komeya, K.; Meguro, T.; Kubota, Y.; Nakahira, A. Top-down tuning of nanosized ZSM-5 zeolite catalyst by bead milling and recrystallization. *Cryst. Growth Des.* **2011**, *11*, 5153–5158. [[CrossRef](#)]
14. Tao, Y.; Kanoh, H.; Abrams, L.; Kaneko, K. Mesopore-modified zeolites: Preparation, characterization, and applications. *Chem. Rev.* **2006**, *106*, 896–910. [[CrossRef](#)]
15. Pérez-Ramírez, J.; Verboekend, D.; Bonilla, A.; Abelló, S. Zeolite catalysts with tunable hierarchy factor by pore-growth moderators. *Adv. Funct. Mater.* **2009**, *19*, 3972–3979. [[CrossRef](#)]
16. Zhang, B.; Zhang, Y.; Hu, Y.; Shi, Z.; Azhati, A.; Xie, S.; He, H.; Tang, Y. Microexplosion under microwave irradiation: A facile approach to create mesopores in zeolites. *Chem. Mater.* **2016**, *28*, 2757–2767. [[CrossRef](#)]

17. Choi, M.; Na, K.; Kim, J.; Sakamoto, Y.; Terasaki, O.; Ryoo, R. Stable single-unit-cell nanosheets of zeolite MFI as active and long-lived catalysts. *Nature* **2009**, *461*, 246–249. [[CrossRef](#)]
18. Xu, D.; Ma, Y.; Jing, Z.; Han, L.; Singh, B.; Feng, J.; Shen, X.; Cao, F.; Oleynikov, P.; Sun, H.; et al. π - π interaction of aromatic groups in amphiphilic molecules directing for single-crystalline mesostructured zeolite nanosheets. *Nat. Commun.* **2014**, *5*, 4262. [[CrossRef](#)]
19. Singh, B.K.; Xu, D.; Han, L.; Ding, J.; Wang, Y.; Che, S. Synthesis of single-crystalline mesoporous ZSM-5 with three-dimensional pores via the self-assembly of a designed triply branched cationic surfactant. *Chem. Mater.* **2014**, *26*, 7183–7188. [[CrossRef](#)]
20. Kore, R.; Srivastava, R.; Satpati, B. ZSM-5 zeolite nanosheets with improved catalytic activity synthesized using a new class of structure-directing agents. *Chem. Eur. J.* **2014**, *20*, 11511–11521. [[CrossRef](#)]
21. Na, K.; Jo, C.; Kim, J.; Cho, K.; Jung, J.; Seo, Y.; Messinger, R.J.; Chmelka, B.F.; Ryoo, R. Directing zeolite structures into hierarchically nanoporous architectures. *Science* **2011**, *333*, 328–332. [[CrossRef](#)] [[PubMed](#)]
22. Dhainaut, J.; Daou, T.J.; Bidal, Y.; Bats, N.; Harbuzaru, B.; Lapisardi, G.; Chaumeil, H.; Defoin, A.; Rouleau, L.; Patarin, J. One-pot structural conversion of magadiite into MFI zeolite nanosheets using mononitrogen surfactants as structure and shape-directing agents. *Cryst. Eng. Comm.* **2013**, *15*, 3009–3015. [[CrossRef](#)]
23. Rioland, G.; Albrecht, S.; Josien, L.; Vidal, L.; Daou, T.J. The influence of the nature of organosilane surfactants and their concentration on the formation of hierarchical FAU-type zeolite nanosheets. *New J. Chem.* **2015**, *39*, 2675–2681. [[CrossRef](#)]
24. Kabalan, I.; Rioland, G.; Nouali, H.; Lebeau, B.; Rigolet, S.; Fadlallah, M.-B.; Toufaily, J.; Hamiyeh, T.; Daou, T.J. Synthesis of purely silica MFI-type nanosheets for molecular decontamination. *RSC Adv.* **2014**, *4*, 37353–37358. [[CrossRef](#)]
25. El Hanache, L.; Lebeau, B.; Nouali, H.; Toufaily, J.; Hamieh, T.; Daou, T.J. Performance of surfactant-modified *BEA-type zeolite nanosponges for the removal of nitrate in contaminated water: Effect of the external surface. *J. Hazard. Mater.* **2019**, *364*, 206–217. [[CrossRef](#)]
26. El Hanache, L.; Sundermann, L.; Lebeau, B.; Toufaily, J.; Hamieh, T.; Daou, T.J. Surfactant-modified MFI-type nanozeolites: Super-adsorbents for nitrate removal from contaminated water. *Microporous Mesoporous Mater.* **2019**, *283*, 1–13. [[CrossRef](#)]
27. Lupulescu, A.I.; Rimer, J.D. Tailoring silicalite-1 crystal morphology with molecular modifiers. *Angew. Chem. Int. Ed.* **2012**, *51*, 3345–3349. [[CrossRef](#)]
28. Lupulescu, A.I.; Kumar, M.; Rimer, J.D. A facile strategy to design zeolite L crystals with tunable morphology and surface architecture. *J. Am. Chem. Soc.* **2013**, *135*, 6608–6617. [[CrossRef](#)] [[PubMed](#)]
29. Gaona Gomez, A.; de Silveira, G.; Doan, H.; Cheng, C.-H. A facile method to tune zeolite L crystals with low aspect ratio. *Chem. Commun.* **2011**, *47*, 5876–5878. [[CrossRef](#)]
30. Zhang, H.; Zhao, Y.; Zhang, H.; Wang, P.; Shi, Z.; Mao, J.; Zhang, Y.; Tang, Y. Tailoring zeolite ZSM-5 crystal morphology/porosity through flexible utilization of silicalite-1 seeds as templates: Unusual crystallization pathways in a heterogeneous system. *Chem. Eur. J.* **2016**, *22*, 7141–7151. [[CrossRef](#)]
31. Zhang, W.; Smirniotis, P.G. On the exceptional time-on-stream stability of HZSM-12 zeolite: Relation between zeolite pore structure and activity. *Catal. Lett.* **1999**, *60*, 223–228. [[CrossRef](#)]
32. Rosinski, E.J.; Rubin, M.K. Preparation of ZSM-12 Type Zeolites. U.S. Patent 4,391,785, 5 July 1983.
33. LaPierre, R.B.; Rohrman, A.C.; Schlenker, J.L.; Wood, J.D.; Rubin, M.K.; Rohrbaugh, W.J. The framework topology of ZSM-12: A high-silica zeolite. *Zeolites* **1985**, *5*, 346–348. [[CrossRef](#)]
34. Kokotailo, G.T.; Fyfe, C.A.; Feng, Y.; Grondey, H.; Gies, H.; Marler, B.; Cox, D.E. Powder X-ray diffraction and solid state NMR techniques for zeolite structure determination. In *Studies in Surface Science and Catalysis*; Beyer, H.K., Karge, H.G., Kiricsi, I., Nagy, J.B., Eds.; Catalysis by Microporous Materials Elsevier: Amsterdam, The Netherlands, 1995; Volume 94, pp. 78–100.
35. Pazzuconi, G.; Terzoni, G.; Perego, C.; Bellussi, G. Selective alkylation of naphthalene to 2,6-dimethylnaphthalene catalyzed by MTW zeolite. In *Studies in Surface Science and Catalysis*; Elsevier: Amsterdam, Netherlands, 2001; Volume 135, p. 152. ISBN 978-0-444-50238-4.
36. Pazzuconi, G.; Perego, C.; Millini, R.; Frigerio, F.; Mansani, R.; Rancati, D. Process for the Preparation of 2,6-dimethylnaphthalene Using a MTW Zeolitic Catalyst. U.S. Patent 6,147,270, 14 November 2000.
37. Dugkhuntod, P.; Imyen, T.; Wannapakdee, W.; Yutthalekha, T.; Salakhum, S.; Wattanakit, C. Synthesis of hierarchical ZSM-12 nanolayers for levulinic acid esterification with ethanol to ethyl levulinate. *RSC Adv.* **2019**, *9*, 18087–18097. [[CrossRef](#)]

38. Itani, L.; Valtchev, V.; Patarin, J.; Rigolet, S.; Gao, F.; Baudin, G. Centimeter-sized zeolite bodies of intergrown crystals: Preparation, characterization and study of binder evolution. *Microporous Mesoporous Mater.* **2011**, *138*, 157–166. [[CrossRef](#)]
39. Rioland, G.; Bullo, L.; Daou, T.J.; Simon-Masseron, A.; Chaplais, G.; Faye, D.; Fiani, E.; Patarin, J. Elaboration of FAU-type zeolite beads with good mechanical performances for molecular decontamination. *RSC Adv.* **2015**, *6*, 2470–2478. [[CrossRef](#)]
40. Rioland, G.; Daou, T.J.; Faye, D.; Patarin, J. A new generation of MFI-type zeolite pellets with very high mechanical performance for space decontamination. *Microporous Mesoporous Mater.* **2016**, *221*, 167–174. [[CrossRef](#)]
41. Fawaz, E.G.; Salam, D.A.; Nouali, H.; Deroche, I.; Rigolet, S.; Lebeau, B.; Daou, T.J. Synthesis of binderless ZK-4 zeolite microspheres at high temperature. *Molecules* **2018**, *23*, 2647. [[CrossRef](#)]
42. Tosheva, L.; Valtchev, V.; Sterte, J. Silicalite-1 containing microspheres prepared using shape-directing macro-templates. *Microporous Mesoporous Mater.* **2000**, *35–36*, 621–629. [[CrossRef](#)]
43. Mañko, M.; Vittenet, J.; Rodriguez, J.; Cot, D.; Mendret, J.; Brosillon, S.; Makowski, W.; Galarneau, A. Synthesis of binderless zeolite aggregates (SOD, LTA, FAU) beads of 10, 70 μm and 1mm by direct pseudomorphic transformation. *Microporous Mesoporous Mater.* **2013**, *176*, 145–154. [[CrossRef](#)]
44. Didi, Y.; Said, B.; Cacciaguerra, T.; Nguyen, K.L.; Wernert, V.; Denoyel, R.; Cot, D.; Sebai, W.; Belleville, M.-P.; Sanchez-Marcano, J.; et al. Synthesis of binderless FAU-X (13X) monoliths with hierarchical porosity. *Microporous Mesoporous Mater.* **2019**, *281*, 57–65. [[CrossRef](#)]
45. Said, B.; Cacciaguerra, T.; Tancret, F.; Fajula, F.; Galarneau, A. Size control of self-supported LTA zeolite nanoparticles monoliths. *Microporous Mesoporous Mater.* **2016**, *227*, 176–190. [[CrossRef](#)]
46. Didi, Y.; Said, B.; Micolle, M.; Cacciaguerra, T.; Cot, D.; Geneste, A.; Fajula, F.; Galarneau, A. Nanocrystals FAU-X monoliths as highly efficient microreactors for cesium capture in continuous flow. *Microporous Mesoporous Mater.* **2019**, *285*, 185–194. [[CrossRef](#)]
47. Moukahhal, K.; Daou, T.J.; Josien, L.; Nouali, H.; Toufaily, J.; Hamieh, T.; Galarneau, A.; Lebeau, B. Hierarchical ZSM-5 beads composed of zeolite nanosheets obtained by pseudomorphic transformation. *Microporous Mesoporous Mater.* **2019**, *288*, 109565. [[CrossRef](#)]
48. Moukahhal, K.; Le, N.H.; Bonne, M.; Toufaily, J.; Hamieh, T.; Daou, T.J.; Lebeau, B. Controlled crystallization of hierarchical monoliths composed of nanozeolites. *Cryst. Growth Des.* **2020**, *20*, 5413–5423. [[CrossRef](#)]
49. Moukahhal, K.; Lebeau, B.; Josien, L.; Galarneau, A.; Toufaily, J.; Hamieh, T.; Daou, T.J. Synthesis of hierarchical zeolites with morphology control: Plain and hollow spherical beads of silicalite-1 nanosheets. *Molecules* **2020**, *25*, 2563. [[CrossRef](#)] [[PubMed](#)]
50. Landers, J.; Gor, G.Y.; Neimark, A.V. Density functional theory methods for characterization of porous materials. *Colloids Surf. A* **2013**, *437*, 3–32. [[CrossRef](#)]
51. Mintova, S.; Ristić, A.; Rangu, M.; Novak Tušar, N. *Verified Syntheses of Zeolitic Materials*; Synthesis Commission of the International Zeolite Association: Caen, France, 2016; ISBN 978-0-692-68539-6.
52. Thommes, M.; Cychosz, K.A. Physical adsorption characterization of nanoporous materials: Progress and challenges. *Adsorption* **2014**, *20*, 233–250. [[CrossRef](#)]
53. Galarneau, A.; Mehlhorn, D.; Guenneau, F.; Coasne, B.; Villemot, F.; Minoux, D.; Aquino, C.; Dath, J.-P. Specific surface area determination for microporous/mesoporous materials: The case of mesoporous FAU-Y zeolites. *Langmuir* **2018**, *34*, 14134–14142. [[CrossRef](#)]
54. Galarneau, A.; Villemot, F.; Rodriguez, J.; Fajula, F.; Coasne, B. Validity of the t-plot method to assess microporosity in hierarchical micro/mesoporous materials. *Langmuir* **2014**, *30*, 13266–13274. [[CrossRef](#)]
55. Carvalho, K.T.G.; Urquieta-Gonzalez, E.A. Microporous–mesoporous ZSM-12 zeolites: Synthesis by using a soft template and textural, acid and catalytic properties. *Catal. Today* **2015**, *243*, 92–102. [[CrossRef](#)]
56. Dimitrov, L.; Mihaylov, M.; Hadjiivanov, K.; Mavrodinova, V. Catalytic properties and acidity of ZSM-12 zeolite with different textures. *Microporous Mesoporous Mater.* **2011**, *143*, 291–301. [[CrossRef](#)]

